Environmental Nanotechnology, Monitoring & Management 20 (2023) 100817

Contents lists available at ScienceDirect

Environmental Nanotechnology, Monitoring & Management

journal homepage: www.elsevier.com/locate/enmm

Magnesium oxide loaded mesoporous silica: Synthesis, characterisation and use in removing lead and cadmium from water supplies

Wahran M. Saod [a], Ian W. Oliver [b,*], David F. Thompson [c], Simon Holborn [d], Alessandro Contini [c], Vladimir Zholobenko [c,e]

[a] Department of Chemistry, College of Science, University of Anbar, Ramadi, Iraq
[b] School of Geography, Geology and the Environment, Keele University, United Kingdom
[c] School of Chemical and Physical Sciences, Keele University, United Kingdom
[d] School of Life Sciences, Keele University, United Kingdom
[e] Department of Chemistry, Moscow State University, Russian Federation

ARTICLE INFO

Keywords:
MgO nanoparticles
Mesoporous silica
MCM-41
Heavy metals
Adsorption isotherms
Water treatment

ABSTRACT

Water pollution by potentially toxic elements such as cadmium (Cd) and lead (Pb) is a persistent problem in many parts of the world. It continues to have profound implications for drinking water supplies, wastewater discharge and environmental quality of rivers and lakes. Treatment is routinely needed but is not always accessible or practical for a given location or situation, hence new treatment options are the focus of much research. Nanotechnology has great potential to enhance water purification and decontamination efficiency. Nanomaterials have been shown to efficiently remove organic and inorganic pollutants, including metals, from contaminated waters but they can have a tendency to flocculate and thereby lose removal efficiency. Research aimed at stabilising nanoparticles into matrices such as silica offers a way forward. In this study, mesoporous silica ($mSiO_2$, also referred to as MCM-41) was prepared and loaded with magnesium oxide nanoparticles (MgO-NP) to form a MgO-silica composite (MgO-$mSiO_2$) and characterised using UV–Vis, FTIR, XRD, BET, and SEM techniques. The MgO-NP, $mSiO_2$ and MgO-$mSiO_2$ were then evaluated for their Cd and Pb removal capacity across varying conditions of pH, metal concentration, adsorbent: solution volume ratio and contact time. Sorption data were evaluated using the Freundlich, Langmuir and Temkin isotherm models. The MgO-$mSiO_2$ was found to have a very high sorption capacity across the conditions tested, with >99% Cd removal across pH range 3–9 and >99% Pb removal across pH range 5–9. When tested at pH 6–7, the MgO-$mSiO_2$ achieved nearly 100% adsorption efficiencies across the contact times tested (15–180 min).

1. Introduction

Lead and cadmium are important metal pollutants that are frequently a cause for concern in relation to drinking water, wastewater and water in the wider environment (e.g., rivers, lakes, oceans). They are listed as Priority Substances under the European Union's Water Framework Directive (WFD) and as Priority and Toxic Pollutants under the USA's Clean Water Act. Therefore, they are considered to be among the most dangerous metals commonly found in water (Zhou et al., 2020). Treatment and removal of metal pollutants from water has thus been a research priority for a long time and consequently there are many techniques employed to remove or reduce their concentrations to permissible or acceptable levels. Techniques include chemical precipitation, membrane filtration, coagulation and flocculation, ion exchange, electrochemical treatment, solvent extraction and oxidation. Such techniques can be effective, but can also have disadvantages, including a high energy consumption rate, high general costs, application methods that require large installations, insufficient or inconsistent removal of pollutants when present in large amounts, and the generation of new wastes that require treatment and disposal (Crini and Lichtfouse, 2019). Therefore, many consider adsorption to be the best or most reliable technique to remove metals due to ease of application and low cost, in addition to the high efficiency of removal that can be achieved (Sodipo and Aziz, 2016). A wide range of sorbents are used and the refining and further development and optimisation of sorbents is a rich field of current research. One growing area is the use of nano-sized metal

* Corresponding author.
E-mail address: i.oliver@keele.ac.uk (I.W. Oliver).

https://doi.org/10.1016/j.enmm.2023.100817
Received 19 December 2022; Received in revised form 22 February 2023; Accepted 26 March 2023
Available online 30 March 2023

oxides as sorbents, and in particular magnesium-based metal oxides (MgO-NP) have shown promise with high adsorption efficiencies for metals (Mahdavi et al., 2015; Seif et al., 2019; Mahdavi et al., 2018). Part of the appeal of MgO-NP is their relatively benign impacts on the environment if released and their low solubility in water, which restricts wider environmental redistribution. However, on their own metal nanoparticles can lose effectiveness as sorbents because of aggregation and related processes during water treatment (Crane and Scott, 2012), hence research efforts have been focused on embedding metal nanoparticles into stable matrices such as mesoporous silica, including the synthesis of nanoparticles embedded or coated in these structures (Singh et al., 2017), with a metal compound nanoparticles at the core, such as zinc oxide (Wang et al., 2009; El-Nahhal et al., 2016a), iron oxide (Sodipo and Aziz, 2016; Zhang et al., 2016; Upadhyay et al., 2021); nickel oxide (Wang et al., 2016), or titanium oxide (Sun et al., 2017), and the matrix or shell composed of silica. In addition to increased stability, SiO_2 amended surfaces of metal compounds can have enhanced properties (Wawrzkiewicz et al., 2017; He et al., 2017). For example, a silica shell changes the surface charge of a metal oxide, enhancing adherence and thereby improving the characteristics of composites in general (He et al., 2017). Characterisation of metal oxide – silica composites can improve understanding of the processes involved when sorption of pollutants occurs. Therefore, the aim of our study was to prepare MgO-loaded mesoporous silica nanoparticles (MgO-mSiO_2), characterise them using a range of analytical techniques, and study their effectiveness in the adsorption of lead and cadmium ions from water under various conditions. To fully evaluate the sorption capacity of the generated composites, we also compared the adsorption of lead and cadmium ions by commercially obtained MgO nanoparticles and mesoporous silica (mSiO_2).

2. Materials and methods

2.1. Chemical reagents

The following reagents were used as purchased without further purification or adjustment: magnesium oxide nanopowder <50 nm (MgO-NP), tetraethyl orthosilicate (TEOS) 98%, and cetyltrimethylammonium bromide (CTAB) 95% from Sigma–Aldrich; lead nitrate, $Pb(NO_3)_2$, and cadmium nitrate tetrahydrate, $Cd(NO_3)_2{\cdot}4H_2O$, from BDH-VWR. Ammonia solution (28% NH_3, analytical reagent grade) was purchased from Fisher Scientific.

2.2. Synthesis of mesoporous silica (MCM-41, or mSiO_2)

The MCM-41 silica matrix was synthesised based on a method reported previously (Guthrie and Reardon, Apr. 2008). 50 g TEOS was added to a polyethylene bottle (1L) with 417.5 g high purity deionised water (<18.2 MΩ·cm), 268.5 g NH_3 (28 wt%) and 10.5 g CTAB. The mixture was subjected to stirring for 30 min and then heated for 24 h at 80 °C and subsequently filtered and rinsed with cold ethanol. Finally, the product was dried at 50 °C and calcinated at 500 °C for 3 h following an approach used elsewhere (Dimos et al., 2009).

2.3. Synthesis of MgO loaded mesoporous silica composite (MgO-mSiO_2)

Synthesis of mesoporous silica – magnesium oxide material composite, labelled as MgO-mSiO_2, was prepared similarly to methods reported previously (Wang et al., 2009; El-Nahhal et al., 2016a; Yuan et al., 2013; Pei et al., 2015). Specifically, by dispersing 0.10 g of MgO-NP in 60 mL ethanol and 1.2 mL concentrated ammonia solution (28 wt %) followed by sonication for 1 h. Then 0.30 g CTAB, dissolved in ethanol, was added to the mixture under constant stirring at room temperature. After that, 0.43 mL TEOS was added dropwise to the mixture under constant stirring which was maintained for a further 6 h. The product was separated from solution by centrifugation (4000 rpm) and washed with deionized water and a few drops of 2 M HCl to remove any excess MgO on the outside surfaces of the MgO-mSiO_2 composite. The product was dried at 100 °C for 12 h and calcined at 500 °C for 3 h.

2.4. Characterization of MgO-mSiO_2, MgO-NP, and mSiO_2

A detailed structural characterisation of the generated mSiO_2 and MgO-mSiO_2, as well as of the commercially obtained MgO-NP, was carried out prior to the sorption studies. UV–vis spectrophotometry (UV-Cary 60, Agilent) was performed on materials dispersed in glycerine and water suspensions. Powder X-ray diffraction (XRD) patterns were recorded on a Bruker D8 Advance diffractometer with CuKα radiation at 40 kV and 40 mA over the 2-theta angle range of 5-70°. The crystalline phases were matched by comparing the XRD patterns of the materials with those reported in the literature. The apparent surface areas of the catalysts were calculated using the BET model for the P/P_0 relative nitrogen pressure <0.15; their pore volume and the pore size distribution were computed using the nonlinear density functional theory (NLDFT) model applied to the adsorption branch of the isotherms obtained from the nitrogen adsorption experiments carried out on a Quantachrom iQ Autosorb instrument. The activation parameters were determined by thermogravimetric analysis (TGA). The TGA analysis was carried out in flowing nitrogen using a Rheometric Scientific STA 1500 instrument; the sample weight change was measured as a function of temperature (ramped from 20 to 800 °C at 10 °C/min). FTIR spectra were monitored using a Thermo iS10 spectrometer equipped with a DTGS detector in the range 6000–1000 cm^{-1} with a spectral resolution of 4 cm^{-1} and 32 scans using an ATR attachment. The obtained infrared spectra were analysed (including subtraction and determination of peak positions) using specialised Thermo software, Omnic. Further details are available elsewhere (Al-Ani et al., 2018; Al-Ani et al., 2020).

2.5. Sorption of lead and cadmium

A batch sorption study was conducted to determine the capacity of the generated MgO-mSiO_2 and mSiO_2, as well as the commercial MgO-NP, to remove Cd and Pb from water under varying conditions of pH (3–9), contact time (15–180 min), adsorbent amount (10–80 mg in 25 mL solution), and initial metal concentration (10–100 mg/L). All experiments were carried out in centrifuge tubes (50 mL) by adding 25 mL solutions containing varied Cd^{2+} and Pb^{2+} concentrations. The samples were shaken (100 rpm, orbital shaker) for the allotted time to provide good contact between adsorbent and adsorbate. Post shaking, the mixtures were centrifuged (5000 rpm) for 10 min to separate the supernatant liquid, which was then analysed for Cd and Pb via inductively coupled plasma optical emission spectroscopy (VISTA-MPX, Agilent). The removal efficiency (%R) and the adsorption capacity at equilibrium (q_e, mg/g) were calculated according to Eq. (1) and Eq. (2).

$$\%R = 100 \times (C_o - C_e)/C_o \quad (1)$$

$$q_e = (C_o - C_e)\ V\ /m \quad (2)$$

where C_o is initial (original) and C_e the final (equilibrium) concentration of metal (mg/L), respectively, m is mass of adsorbent (g) and V the volume of solution (L).

Sorption isotherms (Langmuir, Freundlich and Temkin) were obtained for batch tests using 25 mg adsorbent and metal concentrations spanning 0–100 mg/L. The linear forms of the isotherm equations are presented in equations 3–5 (Langmuir, Freundlich and Temkin, respectively) (Dąbrowski, 2001; Ayawei et al., 2015; Ho, 2006).

$$1/q_e = (1/(K_L\ q_m))\ (1/C_e) + 1/\ q_m \quad (3)$$

$$log\ q_e = log\ K_F + (1/n)\ log\ C_e \quad (4)$$

$$q_e = B_T log\ A_T + B_T log\ C_e \quad (5)$$

where K_L and q_m are the Langmuir constant and the associated maximum monolayer coverage capacity, respectively, K_F is the Freundlich constant and 1/n a dimensionless function of the Freundlich model linked to the strength of adsorption, while A_T is the Temkin isotherm equilibrium constant and B_T a Temkin constant related to heat of sorption (Zhou et al., Nov. 2022).

3. Results and discussion

3.1. Characterisation of optical, morphological and structural properties

3.1.1. UV – Vis spectroscopy

The UV–vis spectra of MgO-NP and mesoporous silica – magnesium oxide composite (MgO-mSiO_2) are shown in Fig. 1. The spectra indicate that both materials have a peak at ~270 nm, which is typical for magnesium oxide (Moorthy et al., 2015).

3.1.2. Fourier transform infrared spectroscopy

The FT-IR spectra of MgO-mSiO_2, MgO-NP and mSiO_2 materials (Fig. 2) show notable peaks within the ranges of 3300–3700 cm^{-1}, 1400–1700 cm^{-1} and 1000–800 cm^{-1}. The mSiO_2 spectrum shows a peak at ~1000 cm^{-1} that is characteristic of Si-O stretching vibrations in silicates and mesoporous silica (Holmes et al., 1998). The MgO-NP has a sharp peak at ~3700 cm^{-1} due to the O-H stretching vibrations and a broad peak at ~1450 cm^{-1} which can be attributed to the bending vibrations of adsorbed water or Mg-OH groups, these have been noted previously for MgO (Balakrishnan et al., 2020); this assignment is also supported by our data for MgO and $Mg(OH)_2$ presented in Fig. S1 (see Supporting Information, SI). The MgO-mSiO_2 has a set of peaks across the range 1420 cm^{-1} to 1624 cm^{-1}; these may reflect the formation of Mg-carbonate and its incorporation into MgO-mSiO_2. Indeed, carbonates are known to have absorption peaks in this region, e.g. hydromagnesite ($Mg_5(CO_3)_4(OH)_2{\cdot}4H_2O$) shows peaks at 1424 and 1482 cm^{-1} (Janet et al., n.d). It is possible that reactions between MgO surfaces, carbon dioxide and water in the air (which can readily occur and has even been proposed as a climate change mitigation option (McQueen et al., Dec. 2020) has led to the Mg-carbonate formation on MgO-NP surfaces to some degree. The FTIR spectrum for $MgCO_3$ measured under the same conditions (Fig. S1) supports this hypothesis.

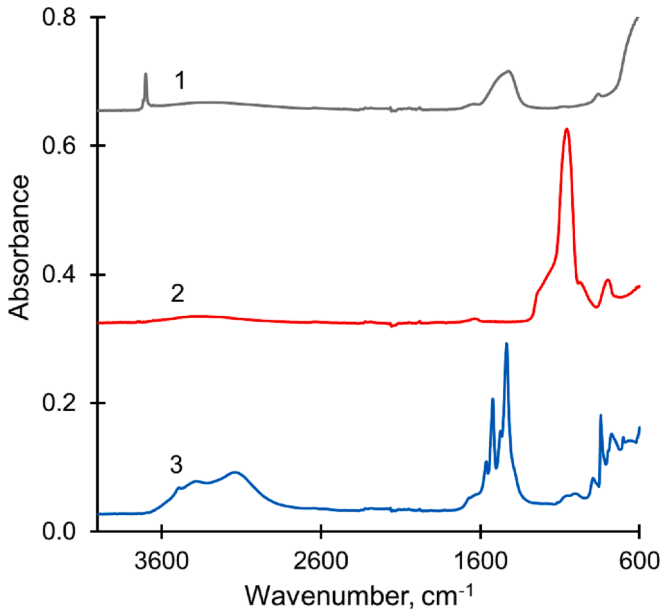

Fig. 2. FTIR spectra of MgO-NP (1), mSiO_2 (2) and MgO-mSiO_2 (3).

3.1.3. X-ray diffraction

The X-ray diffraction (XRD) patterns, which indicate crystal structure and the location of atoms in the lattice structure, for the MgO-mSiO_2, MgO-NP and mSiO_2 are presented in Fig. 3. The XRD pattern of the mSiO_2 exhibits very broad peaks at ~5° and 23°. In addition, small-angle X-ray scattering pattern shows an intense peak corresponding to 3.5 nm d-spacing. This is consistent with the formation of a mesoporous SiO_2 characterised by long-range ordering (e.g. MCM-41 with hexagonal structure) (Zholobenko et al., 2003). Fig. 3 reveals that the XRD pattern of MgO-NP featured major peaks at 37.08°, 43.09°, and 62.57°, which correspond to the known peak positions for MgO (El-Nahhal et al., 2016b; Yuan et al., 2013) and $Mg(OH)_2$ (see Fig. S2a, supplementary information). The MgO-mSiO_2 composite has shown a more complex pattern, with multiple peaks across the 17-40° range. Comparison of

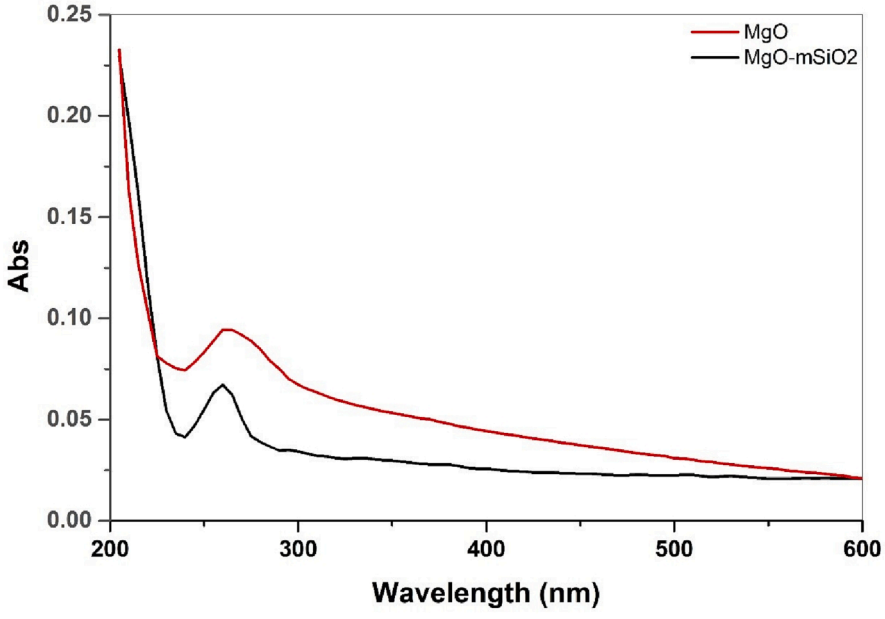

Fig. 1. UV–vis spectra of MgO-mSiO_2 and MgO-NP.

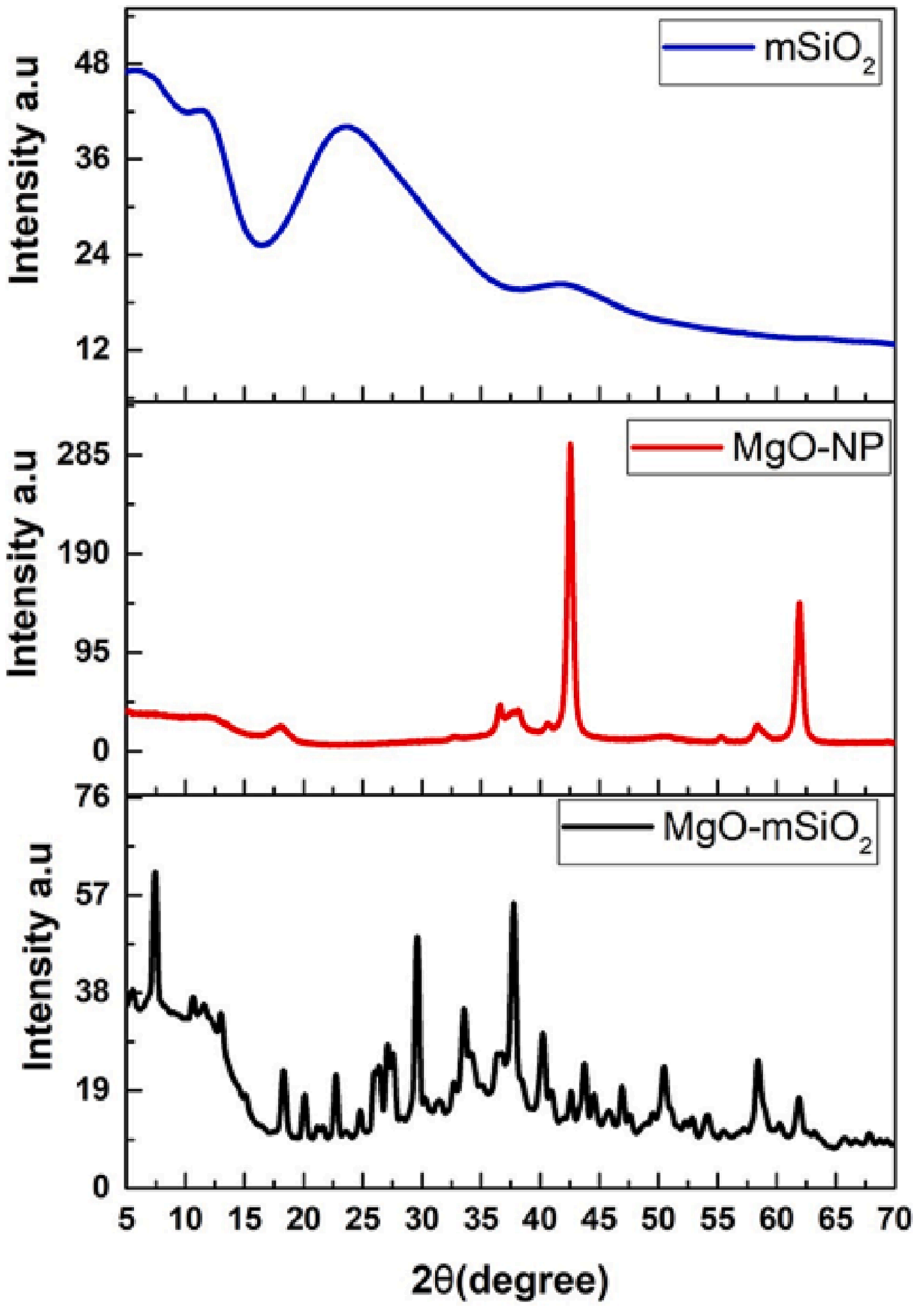

Fig. 3. XRD patterns of MgO-$mSiO_2$, MgO-NP and $mSiO_2$.

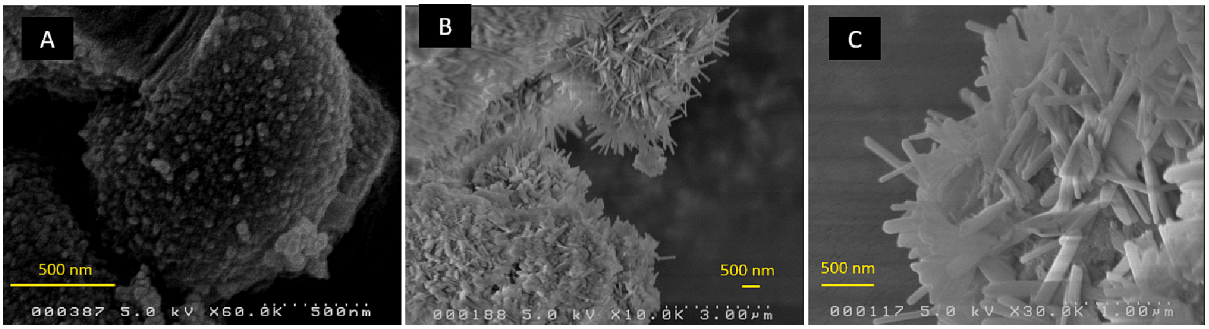

Fig. 4. Scanning electron microscopy (SEM) images for A) synthesised $mSiO_2$ (500 nm), B) MgO-$mSiO_2$ (3000 nm) and C) MgO-$mSiO_2$ (1000 nm). A 500 nm scale bar has been overlain to aid comparison. The contrast in morphology is clear, with synthesised $mSiO_2$, showing amorphous non-crystalline characteristics and the generated MgO-$mSiO_2$ composite having a highly crystalline form.

XRD analysis with the crystallographic databases matched the MgO-$mSiO_2$ pattern to a combination of magnesium silicate hydroxide, magnesium chloride carbonate hydroxide hydrate, and magnesium hydroxide (see Fig. S2b).

3.1.4. Field emission scanning electron microscopy (SEM) analysis

SEM was used to examine surface morphology of the $mSiO_2$, MgO-NP and MgO-$mSiO_2$ (Fig. 4, and Supplementary Fig. S3). The image analysis revealed that the MgO-NP had a shape approaching spherical and a tendency to clump, while the $mSiO_2$, at the resolution examined, shows an amorphous appearance, that is no crystals can be discerned in the images, which is consistent with our XRD data. In contrast, the MgO-$mSiO_2$ had a morphology resembling highly ordered crystal flakes or shards, which is in agreement with the XRD results obtained for this material. The SEM-EDX analysis (Supplementary Fig. S3b) gives an average Mg to Si atomic ratio of 4 for this sample. In addition, the presence of chlorine has been detected, which is consistent with the XRD analysis confirming the formation of magnesium chloride carbonate hydroxide hydrate during the synthesis of MgO-$mSiO_2$.

3.1.5. Thermogravimetric analysis (TGA)

The TGA-DTA curve for $mSiO_2$ (Fig. 5a) has a key feature at 90 °C associated with the loss of physically adsorbed water (24% weight loss) and then a gradual continuous weight loss from that temperature up to 800 °C due to the removal of the surface OH-groups. The data for MgO-NP (Fig. 5b) show an ~5% weight loss around 120 °C, followed by an ~15% mass loss at 330–380 °C. Both processes are endothermic, which is consistent with the desorption of weakly bound water followed by the decomposition of magnesium hydroxide. Based on our data for MgO and $Mg(OH)_2$ presented in Fig. S4, it can be concluded that ~50% of the MgO-NP sample has been hydrated with the formation of magnesium hydroxide and hydrated magnesium oxide. The thermogram of the MgO-$mSiO_2$ (Fig. 5c) indicates a substantial mass loss across a wide temperature range, between 20 and 500 °C. Based on comparison with TGA

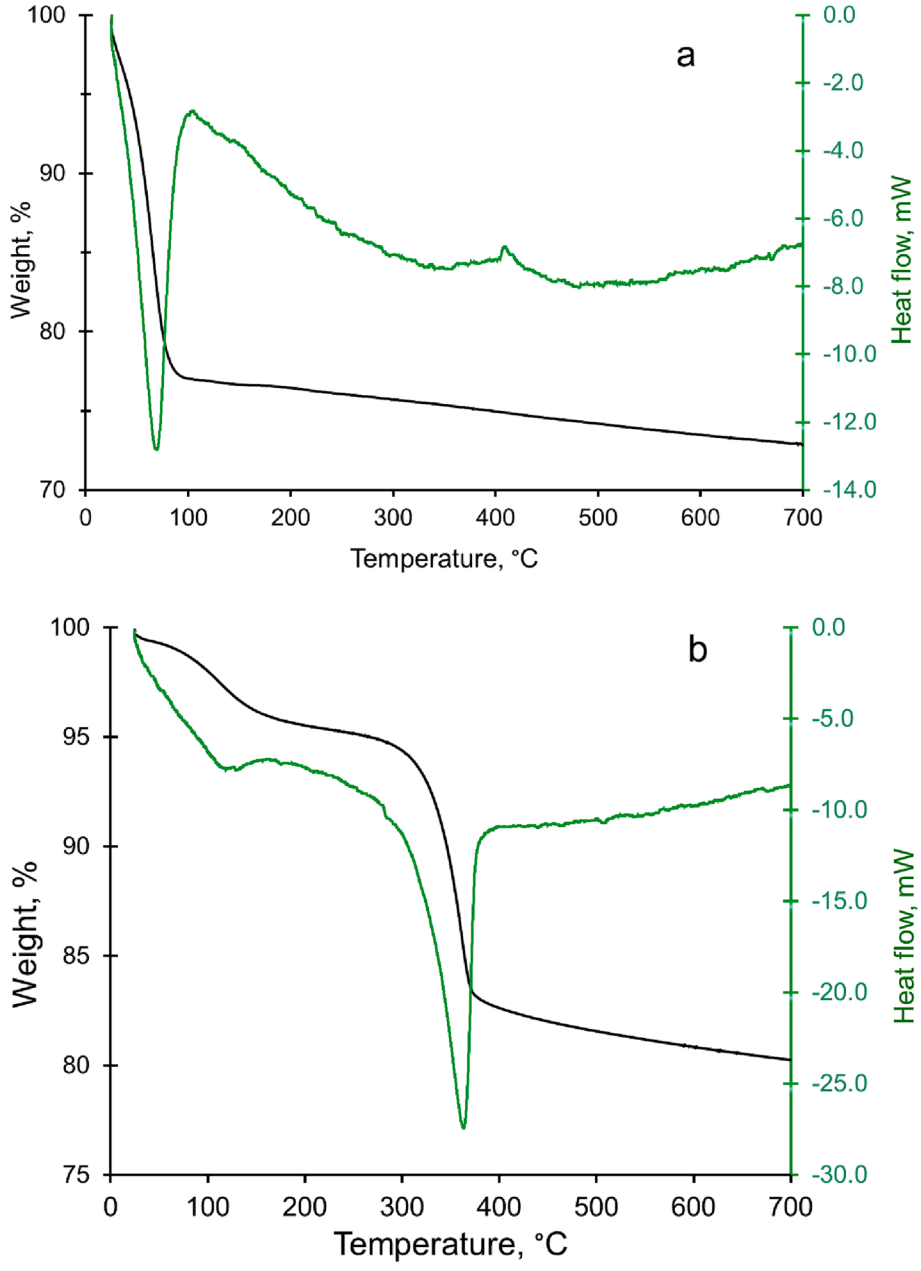

Fig. 5. TGA data for (a) $mSiO_2$, (b) MgO-NP and (c) MgO-$mSiO_2$.

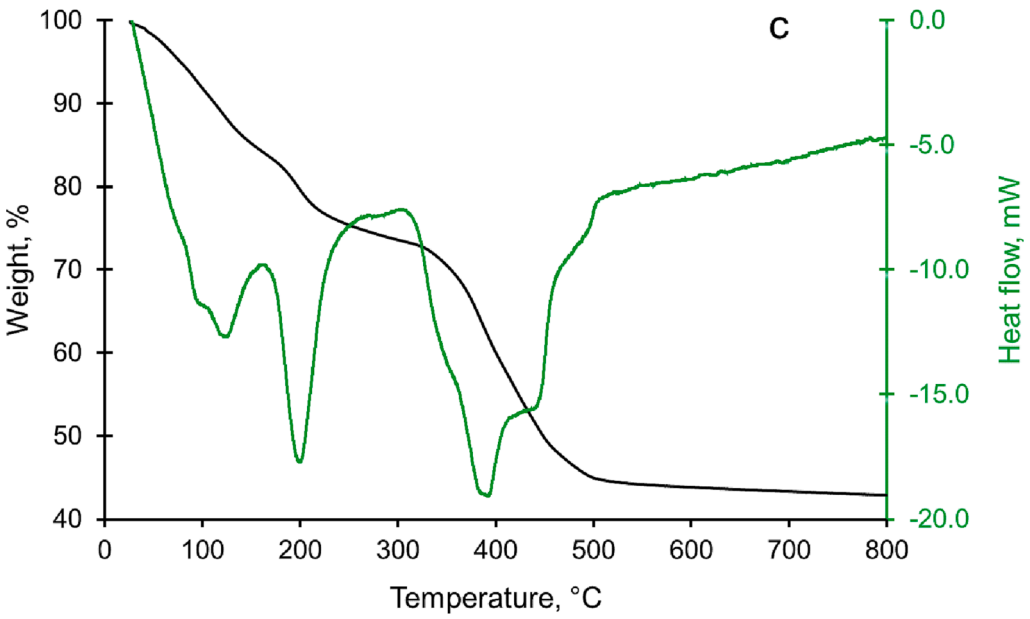

Fig. 5. (*continued*).

data for magnesium carbonates reported in Fig. S4 and the literature data, this can be attributed to the removal of adsorbed water and OH-groups and the decomposition of hydrated $MgCO_3$ and $Mg(OH)_2$ in MgO-$mSiO_2$ (Kitagawa et al., Jul. 2020; Khan et al., 2001). Our data are consistent with the composite MgO-$mSiO_2$ sample containing ~25% of weakly adsorbed water and water of hydration, ~15% of $MgCO_3$, ~40% of $Mg(OH)_2$ and MgO as well as ~20% of mesoporous silica and possibly magnesium silicate.

3.1.6. *Nitrogen adsorption-desorption*

The N_2 sorption isotherms (Fig. 6) show a noticeable nitrogen uptake at a low relative pressure (P/Po < 0.1), which is indicative of a high surface area for this sample, and which is followed by the second step in the N_2 uptake with the relative pressure of ~0.3, which is due to the nitrogen multi-layer adsorption in the mesopores of the MCM-41 type material. The data analysis for $mSiO_2$ shows a narrow pore size distribution peaking at 3.2 nm, with the pore volume of 0.503 cm^3/g and the surface area of 601 m^2/g (Table 1 and supplementary information), which is typical of mesoporous silicas, such as MCM-41 and SBA-15 (Zholobenko et al., 2003). The data analysis for MgO-NP yields the pore volume of 0.115 cm^3/g and surface area of 138 m^2/g. The MgO-NP

Table 1
The pore volume and surface area data obtained for MgO-NP, $mSiO_2$ and MgO-$mSiO_2$.

Material	Surface area (m^2/g)	Pore volume (cm^3/g)
$mSiO_2$	601	0.503
MgO-NP	138	0.115
MgO-$mSiO_2$	78	0.144

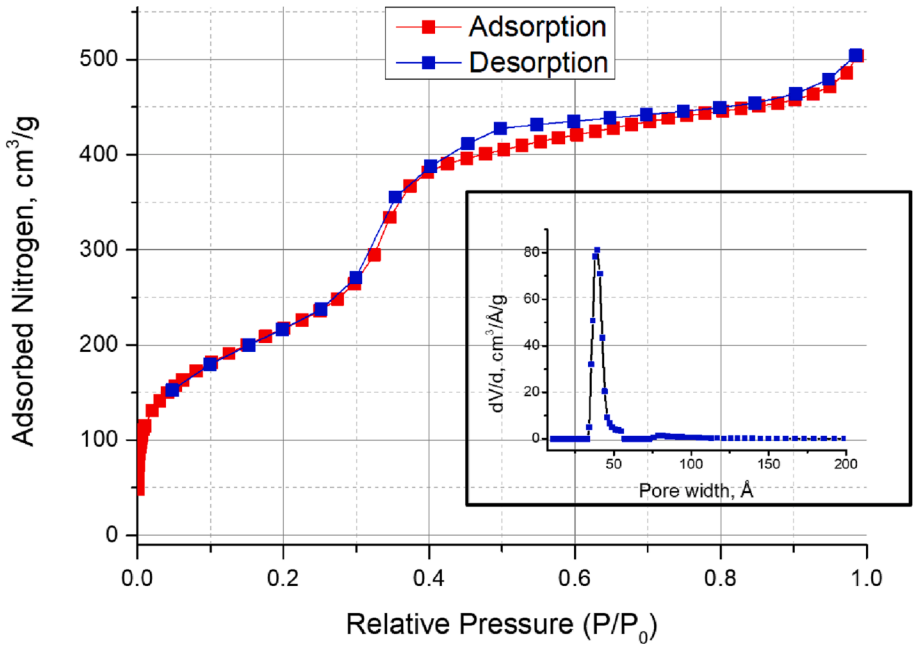

Fig. 6. Nitrogen adsorption-desorption isotherm of $mSiO_2$, and pore size distribution (insert).

sample demonstrates a broad pore size distribution centred around 3 nm (Table 1 and Fig. S5). The MgO-mSiO$_2$ displays the pore volume of 0.144 cm^3/g and a more modest surface area of 78 m^2/g. The pore size distribution for this sample is also broad, with a maximum around 5 nm (Table 1 and Fig. S6). The surface area value for MgO-mSiO$_2$ is much lower than that reported previously (Mohammadi and Naeimi, 2022) for MgO-mSiO$_2$ (619 m^2/g), but still larger than that of the majority of the nanostructured MgO microtubes reported elsewhere (Janet et al., 2007). The lower surface area of the MgO-mSiO$_2$ in the present study may be attributed to the restricted formation of mesoporous silicate in the obtained composite material and the presence of a significant amount of magnesium oxide and carbonate. Future research should investigate this to aid refinement and optimisation of the MgO-mSiO$_2$ synthesis procedure.

3.2. Lead and cadmium adsorption study

3.2.1. Effect of pH

It is widely acknowledged that pH is one of the main factors which controls the adsorption of heavy metal ions, and the results of this study are in line with that premise in that the removal efficiency of Cd and Pb generally decreased as pH decreased, particularly below pH 6 (Fig. 7). Of the three materials tested, the MgO-mSiO$_2$ composite was the only material to effectively maintain 100% removal of Cd across the pH range investigated (i.e. pH range 3–9, with initial metal concentrations of 100 mg/L; Fig. 7). The MgO-mSiO$_2$ composite greatly outperformed the MgO-NP at Cd removal at all pH values below 7, while both consistently removed more Cd than the mSiO$_2$ alone. For Pb, the MgO-mSiO$_2$ composites and the MgO-NP performed equally well at pH 5 and above, removing almost 100% of lead. At pH values of 4 and below the MgO-mSiO$_2$ maintained a slightly higher level of Pb removal than MgO-NP, but at pH 3 achieved approximately the same removal as mSiO$_2$. One important question for future research, from the perspective of material recovery and re-use for multiple rounds of contaminant removal, is whether the MgO remains intact at pH as low as 3 or whether dissolution or other damage occurs. Nevertheless the results show that in keeping with well-established effects of pH on metal sorption, i.e. that at lower pH levels protons compete for sorption sites and cause decreased sorption and increased electrostatic repulsion but that at higher pH values the effects are reversed (Jung et al., Jul. 2018; Fadhel Ali et al., Jan. 2022), the maximum adsorption of 100% removal of both metals was observed for MgO-mSiO$_2$ and MgO-NP at pH 7 to 9, however, for mSiO$_2$ the maximum sorption for Pb was only attained at pH 8 and for Cd at pH 9.

3.2.2. Effect of contact time

In the case of MgO-mSiO$_2$ and MgO-NP, for both Cd and Pb, >99% removal has been achieved across all time periods investigated (15–180 min; Fig. S7). For the mSiO$_2$ alone, the removal efficiency of 55–60% for Pb has been reached after 40 min of equilibration. For Cd, the mSiO$_2$ alone has shown a maximum removal efficiency of ~40% achieved at 15 min of equilibration. The contact time test enables optimal equilibration times to be identified and applied to different water pollution scenarios (i.e. those having different key pollutants or sets of pollutants). Knowing the optimal equilibration time maximises adsorption efficiency (Mudzielwana et al., 2019). As reported elsewhere, optimal removal can sometimes occur within a short equilibration time because at the beginning of the adsorption process the active sites for adsorption on the surface of MgO-mSiO$_2$, MgO and mSiO$_2$ are most vacant (Khan et al., 2020). A decreased efficiency of removal beyond the optimum equilibration can arise due to a decrease in the number of active sites for adsorption on the mesoporous silica, which could be related to the partial degradation of this material.

3.2.3. Effect of adsorbent to solution ratio

The effect of the dose of adsorbent material (i.e. ratio of solid to solution) has been studied with MgO-mSiO$_2$, MgO-NP and mSiO$_2$ (10, 25, 40, 60, and 80 mg per 25 mL) at pH 6–7 and a temperature of 25 °C, with Pb and Cd concentration fixed at 100 mg/L. As shown in Fig. 8, even at the lowest doses of MgO-mSiO$_2$ and MgO-NP (10 mg/25 mL), removal efficiency for both Pb and Cd is >99% (compared with <55% removal of Pb by mSiO$_2$ alone). For mSiO$_2$, in the case of Cd, the highest doses of 60 and 80 mg removed ~85%, while for Pb these doses of mSiO$_2$ removed <65%. It is clear that very high removal rates of Cd and Pb are achieved by MgO-mSiO$_2$ and MgO NPs even at low dose, and while increases from >99% up to 100% removal can be achieved with increasing amounts, the practical significance of the increased removal is minimal to negligible. Such removal capacities are in line with evidence reported and discussed elsewhere (Faisal et al., 2021; Yang et al., 2009; Sherlala et al., 2018).

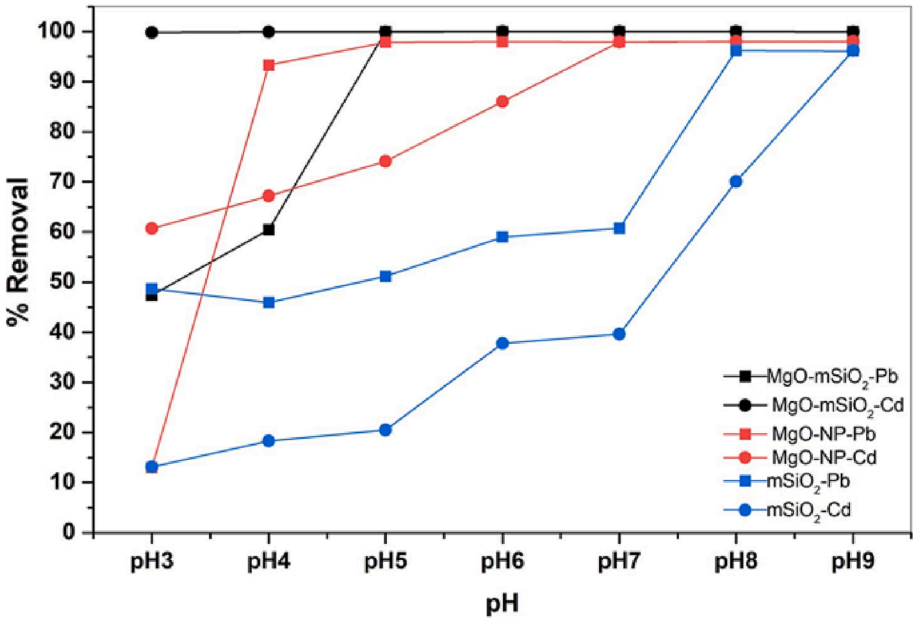

Fig. 7. Effect of pH on Pb and Cd removal, with initial solution concentration 100 mg/L, 25 mg sorbent and 3 h equilibration time (note ~100% removal by MgO-mSiO$_2$ and MgO-NP at pH 5–9; a slight off-set of data points is shown to enable all points to remain visible).

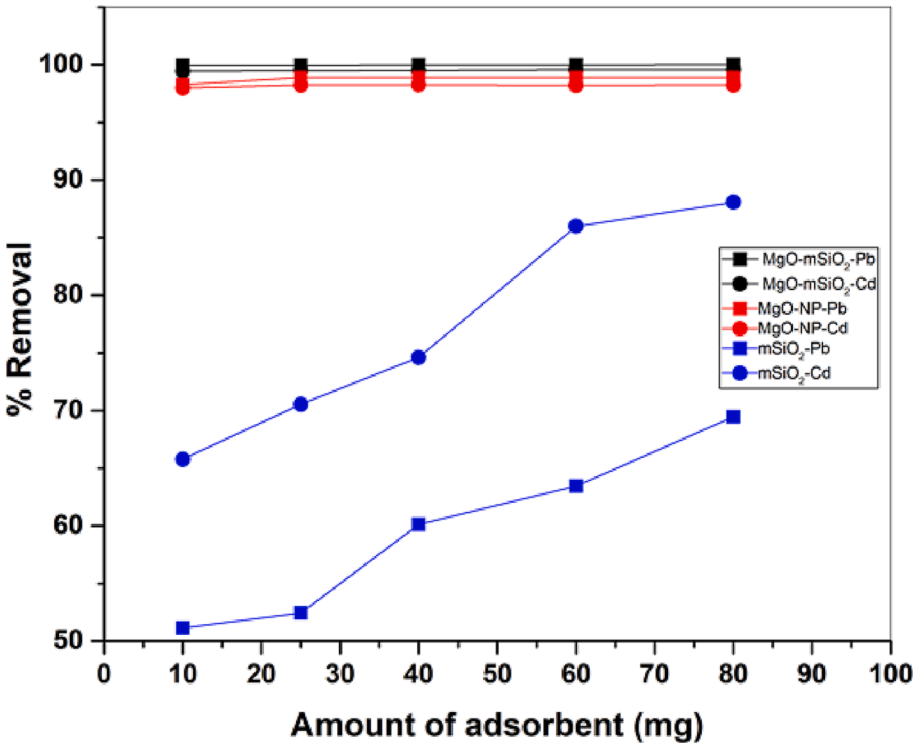

Fig. 8. Effect of adsorbent dose (mass per 25 mL volume) on Pb and Cd removal by the adsorbents, with conditions set at pH 6–7, temperature 25 °C, and Pb and Cd concentration at 100 mg/L (note ~100% removal by both MgO-$mSiO_2$ and MgO-NP at ≥20 mg; a slight off-set of data points is shown to enable all points to remain visible).

3.2.4. Effect of initial solution concentration

At all Cd and Pb concentrations tested (10, 30, 50, 70, and 100) mg/L, the MgO-$mSiO_2$ and MgO-NP removed >99% (Fig. S8). In contrast, the $mSiO_2$ alone had a much more varied removal efficiency, with as low as 10% removal of Cd at 100 mg/L (Fig. S8). The low and variable removal by the $mSiO_2$ is in contrast with what may be expected considering the high surface area and pore space of the material (Table 1), and with results reported elsewhere in which silica nanospheres achieved high removal of Pb (Manyangadze et al., 2020). The results of the present study indicate that, under the conditions tested, the

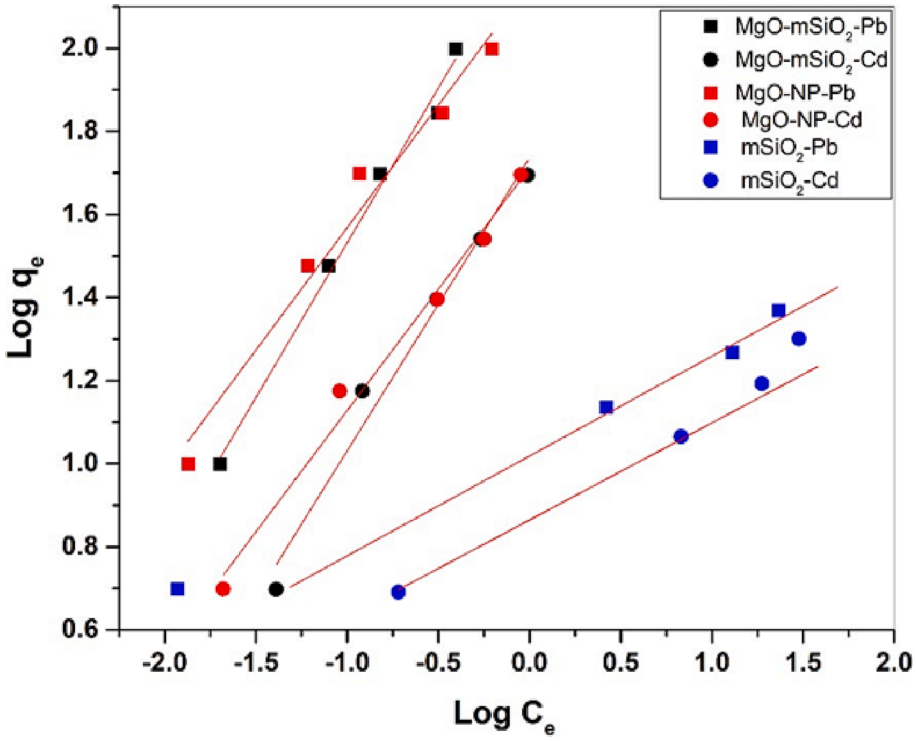

Fig. 9. Freundlich isotherm plots ($\log_{10} q_e$ vs $\log_{10} C_e$) for the removal of lead and cadmium ions by MgO-$mSiO_2$, MgO and $mSiO_2$.

$MgO\text{-}mSiO_2$ and MgO-NP have a stronger affinity for Pb and Cd species than $mSiO_2$.

3.3. Sorption isotherm studies

The linearised Freundlich, Langmuir, and Temkin adsorption isotherms for Pb and Cd conducted at pH 6.0–7.0 are shown in Fig. 9, Figs. S9 and S10, respectively. The individual adsorption isotherm constants and model parameters are presented in the supplementary information (Table S1), and the underlying raw data are presented in Table S2 in the supplementary information. It can be observed that for both Pb and Cd all three models have provided a good fit for the adsorption data on $MgO\text{-}mSiO_2$, MgO-NP and $mSiO_2$ across the concentration range investigated.

The Freundlich model isotherm parameters K_F and 1/n indicate the distribution coefficient and deviation from linearity, respectively (Sparks, 2003), with the latter sometimes also interpreted as an indicator of adsorption intensity. The lower the value of 1/n, the higher is the affinity and heterogeneity of the adsorbent sites. The linearised Freundlich isotherm plots (Fig. 9) and parameter values (Table S1) show that the Freundlich isotherm constant 1/n for Pb and Cd is less than unity for each metal ion, possibly reflecting heterogeneity of surface binding sites. The K_F value for Pb and Cd calculated for $MgO\text{-}mSiO_2$ and MgO-NP are much greater than that for $mSiO_2$, further indicating the greater affinity of $MgO\text{-}mSiO_2$ and MgO-NP for these pollutants.

The Langmuir isotherm model has been chosen for the estimation of maximum adsorption capacity corresponding to complete monolayer coverage on the adsorption surface (Sparks, 2003). The q_m (or q_{max}) parameter is the monolayer coverage at equilibrium in mg/g, whereas K_L is the adsorption equilibrium constant. The Langmuir isotherm plots (Fig. S9) and parameters (Table S1) show that the sorption capacity by the sorbents (q_m) is higher for Pb compared with Cd. The data indicate the high affinity of the ions to bind with $MgO\text{-}mSiO_2$ and MgO-NP, despite $MgO\text{-}mSiO_2$ having lower parameter values revealed by BET analysis. For instance, the q_m value for the adsorption of lead and cadmium on $MgO\text{-}mSiO_2$ are 130 and 82 mg of the metal per 1 g of the composite, whereas for $mSiO_2$, these values are only ~18 and 16 mg/g, respectively. The q_m values for MgO-NP are 96 mg/g in the case of lead and 44 mg/g for cadmium.

The Temkin adsorption isotherms (Fig. S10, Supplementary information) and model parameters (Table S1, Supplementary information) can provide an indication of binding strengths and mechanisms of binding. The Temkin isotherm constant, B_T, related to the heat of sorption, is 21.6, 18.9 and 2.3 kJ/mol for Pb for $MgO\text{-}mSiO_2$, MgO-NP, and $mSiO_2$, respectively. For Cd the values are 11.2, 8.6 and 2.2 kJ/mol, respectively. The results indicate that ion-exchange adsorption mechanisms dominate the sorption processes for $MgO\text{-}mSiO_2$ and MgO-NP, but that rather weak van der Waals interactions take place in the case of Pb and Cd sorption onto $mSiO_2$. Among the three sorbents, in the case of both Cd^{2+} and Pb^{2+}, the Temkin B_T values are highest for $MgO\text{-}mSiO_2$. The Temkin model results also concur with the other models in indicating that Pb^{2+} is subject to a higher affinity sorption than Cd^{2+} onto each of the three sorbents.

4. Conclusions

The synthesised $MgO\text{-}mSiO_2$ has been found to have high sorption capacity for the pollutant metals Cd and Pb across a wide range of pH, solid:solution ratio and contact time. Removal efficiencies have been typically >99% across water pH conditions routinely encountered. Our data demonstrate that the $MgO\text{-}mSiO_2$ material had higher sorption capacity for removing Pb and Cd from water than standard MgO-NP (indicated by higher Langmuir isotherm constants). Both $MgO\text{-}mSiO_2$ and MgO-NP are vastly superior to $mSiO_2$ for Cd and Pb removal at typical pH ranges encountered. Characterisation by UV–vis spectral analysis, FTIR, XRD, nitrogen adsorption-desorption, TGA and SEM analyses have provided a clear understanding of the $MgO\text{-}mSiO_2$ material generated. The $MgO\text{-}mSiO_2$ produced, which can be readily synthesized, presents a promising option for water treatment. Further research into optimisation of the synthesis procedures and post sorption analysis of retained solids should enable additional refinement of the material and elucidation of adsorption mechanisms.

Declaration of Competing Interest

The authors declare that they have no known competing financial interests or personal relationships that could have appeared to influence the work reported in this paper.

Data availability

Data will be made available on request.

Acknowledgements

The authors thank the Ministry of Higher Education and Scientific Research, Iraq, for enabling Wahran Saod to undertake a research sabbatical in the UK. The authors wish to acknowledge analytical support and advice from Richard J. Darton and Jenny Hillman.

Appendix A. Supplementary data

Supplementary data to this article can be found online at https://doi.org/10.1016/j.enmm.2023.100817.

References

Al-Ani, A., Darton, R.J., Sneddon, S., Zholobenko, V., 2018. Nanostructured zeolites: the introduction of intracrystalline mesoporosity in basic faujasite-type catalysts. ACS Applied Nano Materials 1 (1), 310–318.

Al-Ani, A., Freitas, C., Zholobenko, V., 2020. Nanostructured large-pore zeolite: The enhanced accessibility of active sites and its effect on the catalytic performance. Microporous and Mesoporous Materials 293, 109805.

Ayawei, N., Angaye, S.S., Wankasi, D., Dikio, E.D., 2015. Synthesis, Characterization and Application of Mg/Al Layered Double Hydroxide for the Degradation of Congo Red in Aqueous Solution. Open J Phys Chem 05 (03), 56–70. https://doi.org/10.4236/ojpc.2015.53007.

Balakrishnan, G., Velavan, R., Mujasam Batoo, K., Raslan, E.H., 2020. Microstructure, optical and photocatalytic properties of MgO nanoparticles. Results Phys 16, Mar. https://doi.org/10.1016/j.rinp.2020.103013.

Crane, R.A., Scott, T.B., 2012. Nanoscale zero-valent iron: Future prospects for an emerging water treatment technology. Journal of Hazardous Materials 211-212, 112–125.

Crini, G., Lichtfouse, E., 2019. Advantages and disadvantages of techniques used for wastewater treatment. Environ Chem Lett 17 (1), 145–155.

Dąbrowski, A., 2001. Adsorption - From theory to practice. Adv Colloid Interface Sci 93 (1–3), 135–224. https://doi.org/10.1016/S0001-8686(00)00082-8.

Dimos, K., Stathi, P., Karakassides, M.A., Deligiannakis, Y., 2009. Synthesis and characterization of hybrid MCM-41 materials for heavy metal adsorption. Microporous and Mesoporous Materials 126 (1–2), 65–71. https://doi.org/10.1016/j.micromeso.2009.05.021.

El-Nahhal, I.M., Salem, J.K., Kuhn, S., Hammad, T., Hempelmann, R., al Bhaisi, S., 2016a. Synthesis and characterization of silica-, meso-silica- and their functionalized silica-coated copper oxide nanomaterials. Journal of Sol-Gel Science and Technology 79 (3), 573–583. https://doi.org/10.1007/s10971-016-4034-z.

El-Nahhal, I.M., Salem, J.K., Kuhn, S., Hammad, T., Hempelmann, R., al Bhaisi, S., 2016b. Synthesis and characterization of silica coated and functionalized silica coated zinc oxide nanomaterials. Powder Technol 287, 439–446. https://doi.org/10.1016/j.powtec.2015.09.042.

Fadhel Ali, F., Al-Rawi, A.S., Aljumialy, A.M., Jan. 2022. Limestone residues of sculpting factories utilization as sorbent for removing Pb(II) ion from aqueous solution. Results Chem 4, 100621. https://doi.org/10.1016/j.rechem.2022.100621.

Faisal, S., Abdullah, Jan, H., Shah, S.A., Shah, S., Rizwan, M., Zaman, N., Hussain, Z., Uddin, M.N., Bibi, N., Khattak, A., Khan, W., Iqbal, A., Idrees, M., Masood, R., 2021. Bio-catalytic activity of novel mentha arvensis intervened biocompatible magnesium oxide nanomaterials. Catalysts 11 (7), 780.

Guthrie, C.P., Reardon, E.J., Apr. 2008. Metastability of MCM-41 and Al-MCM-41. Journal of Physical Chemistry A 112 (15), 3386–3390. https://doi.org/10.1021/jp710434y.

He, D., Wang, Y., Song, S., Liu, S., Luo, Y., Deng, Y., 2017. Polymer-based nanocomposites employing Bi2S3@SiO2 nanorods for high dielectric performance: Understanding the role of interfacial polarization in semiconductor-insulator core-shell nanostructure. Compos Sci Technol 151, 25–33.

Ho, Y.S., 2006. Second-order kinetic model for the sorption of cadmium onto tree fern: A comparison of linear and non-linear methods. Water Res 40 (1), 119–125. https://doi.org/10.1016/j.watres.2005.10.040.

Holmes, S.M., Zholobenko, V.L., Cundy, C.S., Dwyer, J., 1998. Kinetic investigation of the synthesis of MCM-41 materials. J. Chem. Soc. Faraday Trans. 94, 2025–2032.

C. M. Janet, B. Viswanathan, R. P. Viswanath, and T. K. Varadarajan, "Supporting information Characterization and Photoluminescence Properties of MgO Microtubes Synthesized from Hydromagnesite Flowers.".

Janet, C.M., Viswanathan, B., Viswanath, R.P., Varadarajan, T.K., 2007. Characterization and photoluminescence properties of MgO microtubes synthesized from hydromagnesite flowers. Journal of Physical Chemistry C 111 (28), 10267–10272. https://doi.org/10.1021/jp072539q.

Jung, K.W., Lee, S.Y., Lee, Y.J., Jul. 2018. Hydrothermal synthesis of hierarchically structured birnessite-type MnO2/biochar composites for the adsorptive removal of Cu(II) from aqueous media. Bioresour Technol 260, 204–212. https://doi.org/10.1016/j.biortech.2018.03.125.

Khan, N., Dollimore, D., Alexander, K., Wilburn, F.W., 2001. The origin of the exothermic peak in the thermal decomposition of basic magnesium carbonate. Thermochimica Acta 367–368, 321–333.

Khan, S.A., Siddiqui, M.F., Khan, T.A., 2020. Ultrasonic-assisted synthesis of polyacrylamide/bentonite hydrogel nanocomposite for the sequestration of lead and cadmium from aqueous phase: Equilibrium, kinetics and thermodynamic studies. Ultrasonics Sonochemistry 60, 104761.

Kitagawa, M., Ishida, N., Yoshino, E., Matsuhashi, H., Jul. 2020. Comparison of the base catalytic activity of MgO prepared by thermal decomposition of hydroxide, basic carbonate, and oxalate under atmospheric conditions. Research on Chemical Intermediates 46 (7), 3703–3715. https://doi.org/10.1007/s11164-020-04169-w.

Mahdavi, S., Jalali, M., Afkhami, A., 2015. Heavy metals removal from aqueous solutions by Al2O3 nanoparticles modified with natural and chemical modifiers. Clean Technol Environ Policy 17 (1), 85–102. https://doi.org/10.1007/s10098-014-0764-1.

Mahdavi, S., Molodi, P., Zarabi, M., 2018. Utilization of bare MgO, CeO2, and ZnO nanoparticles for nitrate removal from aqueous solution. Environmental Progress and Sustainable Energy 37 (6), 1908–1917. https://doi.org/10.1002/ep.12865.

Manyangadze, M., Chikuruwo, N.M.H., Narsaiah, T.B., Chakra, C.S., Charis, G., Danha, G., Mamvura, T.A., 2020. Adsorption of lead ions from wastewater using nano silica spheres synthesized on calcium carbonate templates. Heliyon 6 (11), e05309.

McQueen, N., Kelemen, P., Dipple, G., Renforth, P., Wilcox, J., Dec. 2020. Ambient weathering of magnesium oxide for CO2 removal from air. Nat Commun 11 (1). https://doi.org/10.1038/s41467-020-16510-3.

Mohammadi, S., Naeimi, H., 2022. Preparation and Characterization of Hollow MgO/SiO 2 Nanocomposites and Using as Reusable Catalyst for Synthesis of 1 H-isochromenes. Silicon 14, 6881–6893.

Moorthy, S.K., Ashok, C.H., Rao, K.V., Viswanathan, C., 2015. Synthesis and Characterization of Mgo Nanoparticles by Neem Leaves through Green Method. Mater Today Proc 2 (9), 4360–4368. https://doi.org/10.1016/j.matpr.2015.10.027.

Mudzielwana, R., Gitari, W.M., Ndungu, P., 2019. Removal of As(III) from Synthetic Groundwater Using Fe-Mn Bimetal Modified Kaolin Clay: Adsorption Kinetics, Isotherm and Thermodynamics Studies. Environmental Processes 6 (4), 1005–1018. https://doi.org/10.1007/s40710-019-00397-4.

Pei, Y., Wang, M., Tian, D., Xu, X., Yuan, L., 2015. Synthesis of core-shell SiO2@MgO with flower like morphology for removal of crystal violet in water. Journal of Colloid and Interface Science 453, 194–201. https://doi.org/10.1016/j.jcis.2015.05.003.

Seif, S., Marofi, S., Mahdavi, S., 2019. Removal of Cr3+ ion from aqueous solutions using MgO and montmorillonite nanoparticles. Environ Earth Sci 78 (13), 1–10. https://doi.org/10.1007/s12665-019-8380-3.

Sherlala, A.I.A., Raman, A.A.A., Bello, M.M., Asghar, A., 2018. A review of the applications of organo-functionalized magnetic graphene oxide nanocomposites for heavy metal adsorption. Chemosphere 193, 1004–1017. https://doi.org/10.1016/j.chemosphere.2017.11.093.

Singh, S., Kaur, V., Jyoti, Kumar, N., 2017. In: Metal Semiconductor Core-Shell Nanostructures for Energy and Environmental Applications. Elsevier, pp. 35–50.

Sodipo, B.K., Aziz, A.A., 2016. Recent advances in synthesis and surface modification of superparamagnetic iron oxide nanoparticles with silica. Journal of Magnetism and Magnetic Materials 416, 275–291. https://doi.org/10.1016/j.jmmm.2016.05.019.

Sparks, D., 2003. Environmental Soil Chemistry. Academic Press, San Diego.

Sun, J., Xu, K., Shi, C., Ma, J., Li, W., Shen, X., 2017. Influence of core/shell TiO2@SiO2 nanoparticles on cement hydration. Constr Build Mater 156, 114–122. https://doi.org/10.1016/j.conbuildmat.2017.08.124.

Upadhyay, U., Sreedhar, I., Singh, S.A., Patel, C.M., Anitha, K.L., 2021. Recent advances in heavy metal removal by chitosan based adsorbents. Carbohydrate Polymers 251, 117000.

Wang, J., Tsuzuki, T., Sun, L., Wang, X., 2009. Reducing the photocatalytic activity of zinc oxide quantum dots by surface modification. Journal of the American Ceramic Society 92 (9), 2083–2088. https://doi.org/10.1111/j.1551-2916.2009.03142.x.

Wang, H., Zhang, J.F., Bai, Y.X., Wang, W.F., Tan, Y.S., Han, Y.Z., 2016. NiO@SiO2 core-shell catalyst for low-temperature methanation of syngas in slurry reactor. Ranliao Huaxue Xuebao/Journal of Fuel Chemistry and Technology 44 (5), 548–556. https://doi.org/10.1016/s1872-5813(16)30024-x.

Wawrzkiewicz, M., Wiśniewska, M., Wołowicz, A., Gun'ko, V.M., Zarko, V.I., 2017. Mixed silica-alumina oxide as sorbent for dyes and metal ions removal from aqueous solutions and wastewaters. Microporous and Mesoporous Materials 250, 128–147.

Yang, S., Li, J., Shao, D., Hu, J., Wang, X., 2009. Adsorption of Ni(II) on oxidized multi-walled carbon nanotubes: Effect of contact time, pH, foreign ions and PAA. J Hazard Mater 166 (1), 109–116. https://doi.org/10.1016/j.jhazmat.2008.11.003.

Yuan, Q., Li, N., Chi, Y., Geng, W., Yan, W., Zhao, Y., Li, X., Dong, B., 2013. Effect of large pore size of multifunctional mesoporous microsphere on removal of heavy metal ions. J Hazard Mater 254-255, 157–165.

Zhang, J., Chu, C., Sun, A., Ma, S.i., Qiao, X., Wang, C., Guo, J., Li, Z., Xu, G., 2016. Double-sided structural color of Fe3O4@SiO2 nanoparticles under the electric field. J Alloys Compd 654, 251–256.

Zholobenko, V.L., Khodakov, A.Y., Durand, D., 2003. Synchrotron X-ray diffraction-diffusion studies of the preparation of SBA-15 materials. Microporous Mesoporous Materials 66 (2-3), 297–302.

Zhou, X., Maimaitiniyazi, R., Wang, Y., Nov. 2022. Some consideration triggered by misquotation of Temkin model and the derivation of its correct form. Arabian Journal of Chemistry 15 (11), 104267. https://doi.org/10.1016/j.arabjc.2022.104267.

Zhou, Q., Yang, N., Li, Y., Ren, B.o., Ding, X., Bian, H., Yao, X., 2020. Total concentrations and sources of heavy metal pollution in global river and lake water bodies from 1972 to 2017. Glob Ecol Conserv 22, e00925.